Inorganic Chemistry

Article

pubs.acs.org/IC

Detecting Non-bridging Oxygens: Non-Resonant Inelastic X-ray Scattering in Crystalline Lithium Borates

Gérald Lelong,*[,†] Guillaume Radtke,[†] Laurent Cormier,[†] Hanane Bricha,[†] Jean-Pascal Rueff,[‡,§] James M. Ablett,[‡] Delphine Cabaret,[†] Frédéric Gélébart,[†] and Abhay Shukla[†]

[†]Institut de Minéralogie de Physique des Matériaux et Cosmochimie (IMPMC), Sorbonne Universités—UPMC Univ Paris 06, UMR CNRS 7590, Muséum National d'Histoire Naturelle, IRD UMR 206, 4 Place Jussieu, F-75005 Paris, France

[‡]Synchrotron SOLEIL, L'Orme des Merisiers, BP 48, Saint Aubin, 91192 Gif sur Yvette, France

[§]Laboratoire de Chimie Physique-Matière et Rayonnement, Sorbonne Universités-UPMC Univ Paris 06/CNRS-UMR 7614, 75005 Paris, France

ABSTRACT: Probing the local environment of low-Z elements, such as oxygen, is of great interest for understanding the atomic-scale behavior in materials, but it requires experimental techniques allowing it to work with versatile sample environments. In this paper, the local environment of lithium borate crystals is investigated using non-resonant inelastic X-ray scattering (NRIXS) at energy losses corresponding to the oxygen K-edge. Large variations of the spectral features are observed close to the edge onset in the 535−540 eV energy range when varying the Li_2O content. Calculations allow identification of contributions associated with bridging oxygen (BO) and non-bridging oxygen (NBO) atoms. The main result resides in the observed core-level shift of about 1.7 eV in the spectral signatures of the BO and NBO. The clear signature at 535 eV in the O K-edge NRXIS spectrum is thus an original way to probe the presence of NBOs in borates, with the great advantage of making possible the use of complex environments such as a high-pressure cell or high-temperature device for in situ measurements.

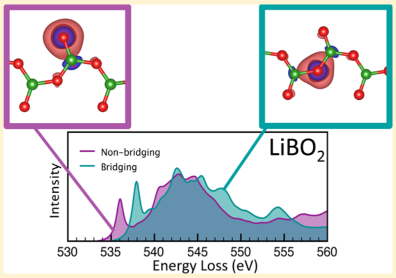

INTRODUCTION

Oxygen is the archetypal *ligand* in crystalline and glassy oxides. It can be found as "bridging" (BO or Ø) or as "non-bridging" (NBO) depending on its connectivity to the network. By definition, a BO is bonded to exactly two network cations. The non-bridging oxygens, which bear a negative charge and are bound to only one network cation, are known to play a key role in ionic transport by acting as a "mediator" during ion migration.[1,2] Moreover, the concentration of NBO is a good indicator of the breakdown of the network connectivity and strongly affects physicochemical properties, such as the diffusivity and viscosity of the relative glasses and melts. Interest for NBOs is high in Materials and Earth Sciences, especially in the understanding of mechanisms involving NBOs in materials placed under extreme conditions (high temperature and/or high pressure).[3,4]

Alkali borate binaries exhibit a richness of crystalline structure spreading over a wide range of alkali oxide content. By taking into account the different known polymorphs, about 75 crystalline alkali borates are presently reported.[5] Their framework structures are all based on BO_3 triangles, BO_4 tetrahedra, or a combination of both. Addition of alkali oxide to pure B_2O_3 converts $\mathrm{B}\varnothing_3$ triangles to negatively charged four-fold coordinated boron units, which causes a widening of the B−Ø−B angle distribution. This conversion is unique to borate systems and results in an increase in network connectivity, contrary to other oxide binaries (silicates, germanates, ...). Above 30−40 mol % alkali oxide content, the $(\mathrm{B}\varnothing_4)^-$ tetrahedra are then replaced by triangular units containing one to three negatively charged NBOs, leading to depolymerization of the borate framework.[6] Though the network structure is usually described in terms of connections between the basic structural units (BO_3 and BO_4), the O sites also reflect the network topology and degree of network polymerization. To fully understand the versatility of the crystalline borate structure and to a second extent the borate glasses and melts, it is essential to detect and understand the role of NBOs.

A variety of spectroscopic techniques has been used to selectively probe the oxygen environment. X-ray photoelectron spectroscopy (XPS) can detect and quantify NBOs in minerals, crystals, and glasses, but this is a surface-sensitive technique requiring ultrahigh vacuum conditions, which often appears as an important limitation for in situ measurements.[7] Electron energy loss spectroscopy (EELS) can be easily used to study the unoccupied states of light elements such as oxygen. Even if some studies have tried to decompose the O K-edge spectrum in BO and NBO components in Ca aluminosilicate glasses or Na borate glasses, no real evidence of a clear and distinguishable spectral signature characteristic of BO or NBO has been found yet.[8,9] Moreover, these type of studies are often hampered by the use of incident high-energy electrons at the origin of important irradiation damage, especially on insulating materials such as borates,[9,10] rendering such studies quite

Received: May 8, 2014
Published: October 2, 2014

dx.doi.org/10.1021/ic501730q | *Inorg. Chem.* 2014, 53, 10903−10908

Table 1. Parameters Employed for Generation of the Pseudopotentials[a]

atom	Li	B	O	O (core−hole)
valence states	$2s^{0.9}$ (1.53) $2p^{0.0}$ (1.53)	$2s^{2.0}$ (0.82) $2p^{0.9}$ (0.82)	$2s^{2.0}$ (0.61) $2p^{4.0}$ (0.61)	$2s^{2.0}$ (0.61) $2p^{4.0}$ (0.61)
local part	s	p	p	p
nonlinear core corrections	yes	no	no	no

[a] The core radii of the valence states are indicated in parentheses in Angstroms.

difficult to achieve. ^{17}O triple-quantum magic angle spinning (3QMAS) and to a second extent ^{11}B multiple quantum magic angle spinning (MQMAS) nuclear magnetic resonance (NMR) are very efficient to discriminate the BOs and the NBOs.[4,11−14] However, use of isotopically enriched samples is a major limitation for studying natural samples or for a systematic study. Furthermore, none of the above techniques are very well suited for in situ high-temperature/high-pressure measurements, although relatively moderate temperature (EELS, NMR)[15,16] and pressure (NMR)[17] ranges can be explored with these techniques.

A promising direction relies on use of the non-resonant inelastic X-ray scattering (NRIXS) to probe the O K-edge. Using high-energy incident X-rays, NRIXS is bulk sensitive and can be used as a substitute for ultrasoft X-ray absorption spectroscopy (USXAS) for K-edges of light elements (B, C, O, ...), since USXAS has a low penetration depth, as all spectroscopic techniques using soft X-rays.[18] Like EELS, the K-edges are obtained in the energy loss domain. However, based on hard X-rays, NRIXS allows the use of complex environments, and recent in situ high-pressure studies at the O and B K-edges clearly demonstrate the potentialities of the technique.[19−23] Contrary to the B K-edge, which is now relatively well understood, specific signatures observed at the O K-edge remain unclear in alkali borates. Unraveling the origins of these features requires therefore a systematic comparison of the experimental data with calculations, similar to what has been done on silicates.[24]

The eight known crystalline structures of the $Li_2O-B_2O_3$ system extend over a wide Li_2O/B_2O_3 ratio, allowing detection of the successive structural evolution: BO_3/BO_4 conversion and the appearance and concentration effect of NBOs as a function of Li content.[5,25,26] The $Li_2O-B_2O_3$ system is thus perfectly suited for a systematic study of the local environment of the oxygen atoms at room temperature, prior to in situ HP and/or HT measurements. By coupling the precise knowledge of the different lithium borate crystalline structures with the experimental NRIXS spectra and theoretical calculations, we are able to finely interpret the oxygen K-edge signals, explore the structural and electronic properties of O−B bonds, and show that the O K-edge can be used as a sensitive probe of the presence of NBOs.

EXPERIMENTAL DETAILS

In order to span a large lithium concentration range, six lithium borate crystals have been prepared with the following molar compositions: $3Li_2O:11B_2O_3$, $Li_2O:2B_2O_3$, $Li_2O:B_2O_3$, $3Li_2O:2B_2O_3$, $2Li_2O:B_2O_3$, and $3Li_2O:B_2O_3$. Lithium borate crystals have been synthesized using the procedure described by Mathews et al.[27] Lithium carbonate Li_2CO_3 and boric acid H_3BO_3 (reagent grade) were mixed in appropriate quantities and placed in a platinum crucible for melting at 1225 K for 15 min. Once melted, the sample is quenched, ground into powder, and finally heated at 823 K for 48 h. A final 1 day thermal treatment is then applied at a temperature between 823 and 1073 K depending on the chemical composition of the sample.

The purity of the crystalline phases for each compound has been checked using powder X-ray diffraction (Cu Kα radiation on a Panalytical X'pert pro MPD). Diffractograms were compared with the literature,[26,28−33] and the following crystalline phases have been identified

$3Li_2O: 11B_2O_3 \rightarrow Li_3B_{11}O_{18}$

$Li_2O: 2B_2O_3 \rightarrow Li_2B_4O_7$

$Li_2O: B_2O_3 \rightarrow \alpha\text{-}LiBO_2$

$3Li_2O: 2B_2O_3 \rightarrow Li_6B_4O_9$

$2Li_2O: B_2O_3 \rightarrow \alpha\text{-}Li_4B_2O_5$

$3Li_2O: B_2O_3 \rightarrow Li_3BO_3$

NRIXS measurements were performed on the GALAXIES beamline at the SOLEIL Synchrotron.[34] Polycrystalline samples were ground into a powder and placed into 2 mm circular holes drilled in the aluminum sample holder. The incident beam was monochromatized with a Si(111) double-crystal monochromator and the beam focused to ~100 (H) × 30 (V) μm^2. Scattered radiation was analyzed with 4 spherical Si(660) analyzers (R = 1 m) and detected with an avalanche photodiode (APD). Spectra were collected by keeping the analyzers fixed at their backscattering energy of 9.720 keV (Bragg angle ≈ 86°) while scanning the incident X-ray energy. For example, the O K-edge at 535 eV was measured by varying the incident X-ray energy around 10.255 keV. The total energy resolution of the setup was ~1.5 eV. All measurements were made at an average scattering angle of 40° in 2θ. Under these conditions all 4 analyzers are in a low exchanged momentum q configuration ($q \approx 3.37$ Å^{-1}), and their signal can be summed. An accumulation time of at least 5 h was necessary to achieve good statistics.

COMPUTATIONAL DETAILS

All calculations presented hereafter have been performed using the suite of codes QUANTUM ESPRESSO[35] based on density-functional theory. Norm-conserving pseudopotentials[36] in the Kleinman−Bylander[37] form have been generated according to the parameters summarized in Table 1 and using the generalized-gradient approximation of Perdew, Burke, and Ernzerhof[38] for exchange and correlation. Particular care has been taken to minimize core overlaps in the presence of short B−O bond lengths (~1.31−1.45 Å) within the BO_3 structural units. Consequently, a cut-off energy of 140 Ry for the plane-wave expansion was necessary to reach a convergence of the total energy better than 1 mRy/atom. The pseudopotential of the oxygen-absorbing atom was obtained by removing one 1s core electron from its electronic configuration.

NRIXS spectra for the O K-edge were calculated in a continued fraction approach[39] using the XSPECTRA module.[40,41] The all-electron final-state wave function of the absorbing atom was reconstructed using two p projectors within the projector-augmented wave method.[42] Although this module is primarily intended to model X-ray absorption spectroscopy, its use for NRIXS remains valid as long as dipole-allowed electronic transitions dominate higher order terms. In our experimental conditions (i.e., in the low-q regime), the argument (qr) of the exponential operator appearing in the expression of the NRIXS dynamical structure factor[18] remains indeed well below unity (for an O 1s orbital mean radius $\langle r \rangle \approx 0.1$ Å and $qr \ll 1$), justifying therefore this approximation.

Table 2. Description of the Supercells Employed for the Self-Consistent Field and NRIXS Spectra Calculations[a]

compound	cryst struct	supercell	k-point grid	no. of inequivalent O sites	shortest distance between absorbing atoms
$Li_3B_{11}O_{18}$	ref 26	1 × 1 × 1 (128 atoms)	2 × 5 × 4	18	7.79
$Li_2B_4O_7$	ref 29	1 × 1 × 1 (104 atoms)	4 × 4 × 3	4	9.47
α-$LiBO_2$	ref 31	2 × 2 × 2 (128 atoms)	3 × 4 × 3	2	8.71
$Li_6B_4O_9$	ref 26	3 × 1 × 1 (228 atoms)	4 × 2 × 4	9	9.17
α-$Li_4B_2O_5$	ref 30	1 × 2 × 1 (176 atoms)	3 × 4 × 2	10	9.47
α-Li_3BO_3	ref 33	3 × 1 × 1 (84 atoms)	4 × 4 × 5	3	8.31

[a]The shortest distance between absorbing atoms is given in Angstroms.

For each compound, the resulting spectra have been calculated according to the following procedure. In a first step, the individual spectra corresponding to each crystallographically inequivalent oxygen site in the unit cell were calculated in the full core−hole (FCH) approximation, i.e., by including a single oxygen absorbing atom in a supercell and by accounting for the photoelectron through an additional uniform background charge. These calculations have been performed using the experimental crystal structures reported in the literature. Use of supercells was necessary to provide a sufficient spatial separation (∼8 Å) between the absorbing atom and its periodically repeated images and thus to avoid any spurious interactions. A summary of the supercells employed for the different compounds under study is shown in Table 2 together with the corresponding k-point Monkhorst−Pack grids used for both self-consistent field and NRIXS spectra calculations. A constant broadening parameter of 1 eV has been used in the continued fraction. This broadening was deliberately set to a lower value than the experimental resolution to allow for a better visualization of fine spectral features.

For each compound, the *relative* core-level shifts between individual spectra have been evaluated in a second step. First, the energies of the lowest unoccupied state for each individual spectra calculated in the FCH approximation have been aligned. Then, the excitation energies corresponding to each inequivalent oxygen atomic site have been computed as the total supercell energies in the excited core−hole (XCH) approximation, i.e., by promoting the photoelectron in the lowest available conduction state. In these two steps, the oxygen site with the lowest excitation energy has been taken as the reference site. Finally, the relative core-level shifts, corresponding to the differences between these excitation energies, were applied to each individual spectra. In a given compound, for which site i is the reference site, the calculated spectrum for site j was therefore shifted by the energy

$$\begin{aligned}\Delta^j_{\mathrm{CLS}} &= E^j_{\mathrm{XCH}} - E^i_{\mathrm{XCH}} + \epsilon^i_{\mathrm{FCH}} - \epsilon^j_{\mathrm{FCH}}\\ &= (E^j_{\mathrm{XCH}} - \epsilon^j_{\mathrm{FCH}}) - (E^i_{\mathrm{XCH}} - \epsilon^i_{\mathrm{FCH}})\end{aligned}$$

where E^k_{XCH} is the total supercell energy calculated in the XCH approximation for an absorber atom located in site k and $\epsilon^k_{\mathrm{FCH}}$ is the energy of the lowest unoccupied state calculated in the FCH approximation for an absorber atom located in the same site. This approach is known to provide accurate alignments of spectra arising from distinct inequivalent sites within a given crystal and a set of calculations performed in the same, sufficiently large, supercell.[43] In a final step, the O K-edge spectrum was obtained as a weighted average of these individual components accounting for the multiplicity of each oxygen atomic site.

■ RESULTS AND DISCUSSION

The phase diagram of the $Li_2O-B_2O_3$ system is extremely rich in crystalline structures. Even though it has been explored over the last five decades, some structures have been only resolved very recently, such as $Li_3B_{11}O_{18}$, $Li_6B_4O_9$, and $Li_4B_2O_5$ compounds.[26,30] The wide range of accessible compositions opens the possibility to closely follow the evolution of network topologies upon addition of lithium oxide into pure B_2O_3. Figure 1 shows a complete overview of the 6 crystalline compounds studied in this paper. Below 33 mol % of Li_2O, the crystalline structures are fully polymerized and composed of $BØ_3$ triangular and $BØ_4$ tetrahedral units, corresponding to three-fold $^{[3]}B$- and four-fold $^{[4]}B$-coordinated boron atoms, respectively. The proportion of four-fold $^{[4]}B$-coordinated boron atoms increases monotonically to reach the maximum value of 50 mol % for $Li_2B_4O_7$. In this latter compound, two $BØ_4$ units are linked together by vertices. Beyond 33 mol %, all $BØ_4^-$ units disappear abruptly in favor of NBOs and triangular units. As a consequence, all remaining crystals are composed exclusively of three-fold-coordinated boron atoms linked or not by vertices though Ø. The concentration of NBOs increases linearly from $LiBO_2$ to Li_3BO_3 following a reduction of dimensionality caused by depolymerization of the network.[26]

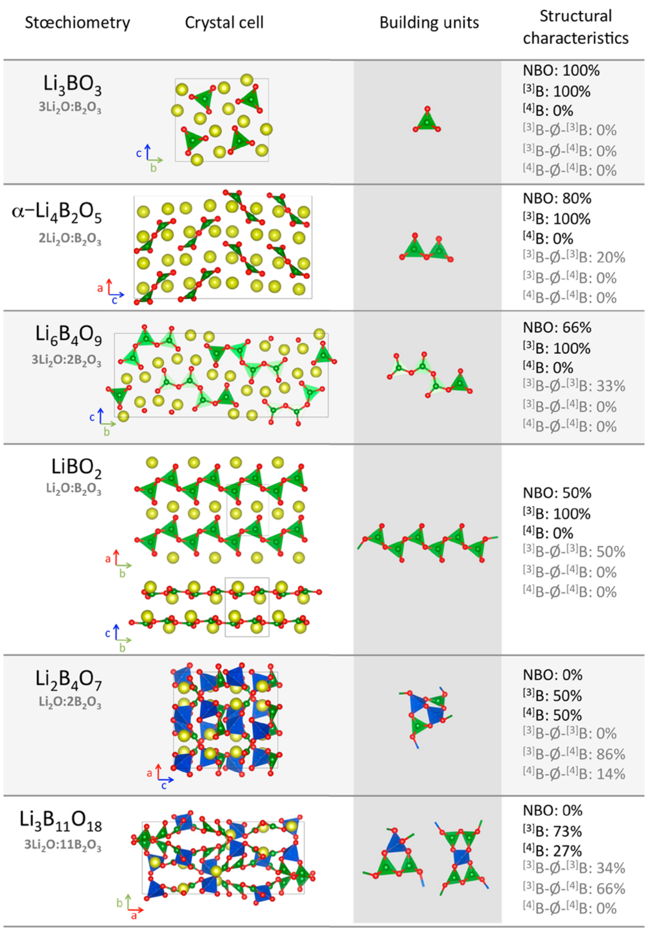

Stœchiometry	Crystal cell	Building units	Structural characteristics
Li_3BO_3 $3Li_2O{:}B_2O_3$			NBO: 100% $^{[3]}B$: 100% $^{[4]}B$: 0% $^{[3]}B$-Ø-$^{[3]}B$: 0% $^{[3]}B$-Ø-$^{[4]}B$: 0% $^{[4]}B$-Ø-$^{[4]}B$: 0%
α-$Li_4B_2O_5$ $2Li_2O{:}B_2O_3$			NBO: 80% $^{[3]}B$: 100% $^{[4]}B$: 0% $^{[3]}B$-Ø-$^{[3]}B$: 20% $^{[3]}B$-Ø-$^{[4]}B$: 0% $^{[4]}B$-Ø-$^{[4]}B$: 0%
$Li_6B_4O_9$ $3Li_2O{:}2B_2O_3$			NBO: 66% $^{[3]}B$: 100% $^{[4]}B$: 0% $^{[3]}B$-Ø-$^{[3]}B$: 33% $^{[3]}B$-Ø-$^{[4]}B$: 0% $^{[4]}B$-Ø-$^{[4]}B$: 0%
$LiBO_2$ $Li_2O{:}B_2O_3$			NBO: 50% $^{[3]}B$: 100% $^{[4]}B$: 0% $^{[3]}B$-Ø-$^{[3]}B$: 50% $^{[3]}B$-Ø-$^{[4]}B$: 0% $^{[4]}B$-Ø-$^{[4]}B$: 0%
$Li_2B_4O_7$ $Li_2O{:}2B_2O_3$			NBO: 0% $^{[3]}B$: 50% $^{[4]}B$: 50% $^{[3]}B$-Ø-$^{[3]}B$: 0% $^{[3]}B$-Ø-$^{[4]}B$: 86% $^{[4]}B$-Ø-$^{[4]}B$: 14%
$Li_3B_{11}O_{18}$ $3Li_2O{:}11B_2O_3$			NBO: 0% $^{[3]}B$: 73% $^{[4]}B$: 27% $^{[3]}B$-Ø-$^{[3]}B$: 34% $^{[3]}B$-Ø-$^{[4]}B$: 66% $^{[4]}B$-Ø-$^{[4]}B$: 0%

Figure 1. Structural description of the six studied crystals in the $Li_2O-B_2O_3$ binary. Lithium atom, oxygen atom, BO_3 triangles, and BO_4 tetrahedra are colored in yellow, red, green, and blue, respectively. The crystal structure, the constituting units describing the environment of oxygen and boron atoms, and a summary of the coordination of each compound are given.

The O K-edge NRIXS spectra of the six crystalline compounds $Li_3B_{11}O_{18}$, $Li_2B_4O_7$, $LiBO_2$, $Li_6B_4O_9$, $Li_4B_2O_5$, and Li_3BO_3 accompanied by vitreous v-B_2O_3 are shown in Figure 2.

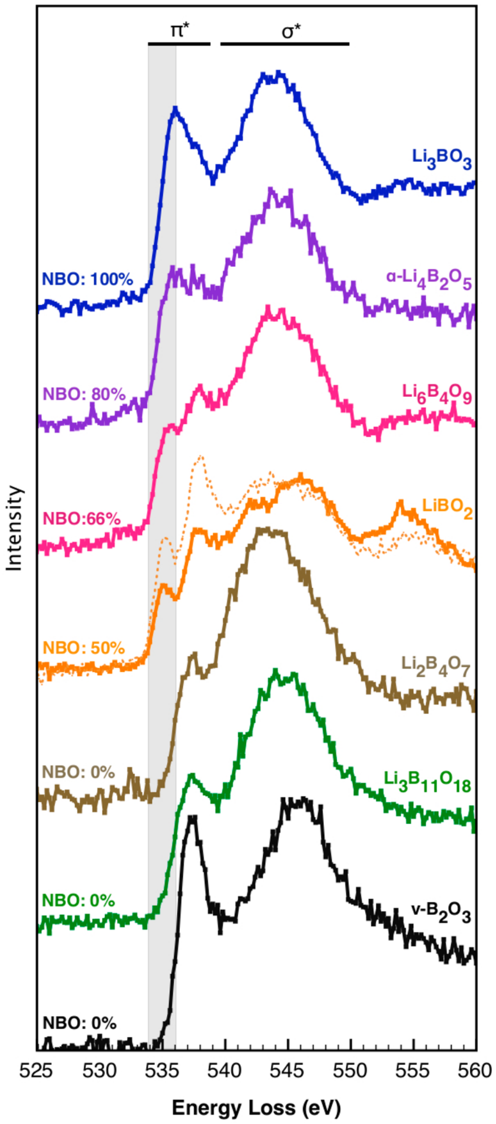

Figure 2. O K-edge NRIXS spectra for the six crystalline compounds of the $Li_2O-B_2O_3$ system. Li content increases from bottom to top, starting from a Li_2O concentration of 21 mol % in $Li_3B_{11}O_{18}$ (green) to 75 mol % in Li_3BO_3 (blue). O K-edge spectrum of vitreous B_2O_3 (black) is shown as an example of a pure 3-fold-coordinated boron in a fully coordinated network. Gray-colored area around 535 eV indicates the spectral signature of the non-bridging oxygens (NBO). Proportion of NBO is also given for each composition. Two O K-edge spectra of $LiBO_2$ (plain line and dashed line) were measured at two different orientations.

Due to the lamellar structure of $LiBO_2$, preferential orientations of the crystalline powder of $LiBO_2$ are adopted in the sample holder (See Figure 1). In order to illustrate this point, two O K-edge spectra of $LiBO_2$ are presented in Figure 2 recorded on the oriented powder and on a bulk polycrystalline sample. Though the peaks do not change in position, it is difficult to assess the exact relative intensities of the main features composing the isotropic O K-edge NRIXS spectrum.

v-B_2O_3 is used here as a reference of a fully polymerized network composed only of bridging oxygens (Ø) and $BØ_3$ units. Unambiguously, addition of alkali cations leads to large changes in the O K-edge spectra. The O K-edge spectrum of v-B_2O_3 (0% NBO) is composed of a narrow peak at 537 eV and a broader one around 546 eV, corresponding, respectively, to electronic transitions from a 1s core state to unoccupied antibonding π^* and σ^* orbitals of the BO_3 structural units. Both peaks are related to two-fold-coordinated oxygen atoms with a relatively narrow $^{[3]}B-Ø-^{[3]}B$ angle dispersion.[19] The spectrum of Li_3BO_3 (100% NBO) is similarly simple with a broader and shifted π^* peak. In between, upon addition of lithium oxide, considerable changes occur. First, the intensity of the narrow peak at 537 eV decreases until $Li_2B_4O_7$, and simultaneously, the broad peak shifts to lower energies (543 eV). Both changes coincide with the appearance and increase of the concentration of $^{[4]}B$ atoms. Substitution of a planar BO_3 triangle to a BO_4 tetrahedron modifies strongly the topology by widening the angular B−Ø−B distribution and increasing the Ø−B bond lengths. Second, for the four crystals with the highest Li content, an additional peak appears at 535 eV, whose intensity increases with the alkali content and the appearance of the NBO species. Conversely, the intensity of the peak at 537 eV decreases continuously, and this peak almost disappears in the case of Li_3BO_3.

The calculated O K-edge spectra are compared to the experimental NRIXS data in Figure 3 for the series of crystals under study. An energy shift of 535 eV has been applied to all theoretical spectra to match the experiments. Simulations reproduce well the overall shape of the experimental spectra, dominated by electronic transitions from the 1s core state to the narrow π^* and broader σ^* antibonding states associated with the BO_3 structural units.

The major insight brought by these calculations resides in the explanation of the large variations of the spectral features observed close to the edge onset, in the 535−540 eV energy range. On considering the decomposition of the theoretical spectrum into separate contributions associated with the BO and the NBO atoms, as shown in Figure 3, the transitions to π^* states can be unequivocally separated into contributions from these two species, thus providing an experimental signature for the presence of each species. This is the central result of our work.

Although the oxygen K-edge is sensitive to the complex electronic structure associated with the short- and extended-range structures, the peak observed at 535 eV can be interpreted in the first approximation as arising from transitions to π^* states of oxygen in BO_3 structural units and is associated with NBO atoms, whereas the peak located at 537 eV is related to transitions toward the same antibonding states but associated with the bridging oxygen atoms. Decomposition of the O K-edge further shows that the relative intensities of these two peaks are closely related to the NBO/BO ratio present in each crystal structure. For low Li contents ($Li_3B_{11}O_{18}$ and $Li_2B_4O_7$), NBOs are absent and a unique peak arising from BOs is observed at 537 eV. A further increase of the Li concentration leads to the appearance of NBOs with increasing numbers of NBO on moving from α-$LiBO_2$ to $Li_6B_4O_9$ and α-$Li_4B_2O_5$. Correspondingly, the intensity of the 535 eV peak increases with respect to the intensity of the 537 eV peak. This effect is particularly well reproduced in the calculations. In the limiting case of Li_3BO_3, the low energy loss contribution of NBOs explains the shape of the experimental spectrum.

A qualitative explanation of the origin of this core-level shift can be found in the very different chemical environment of

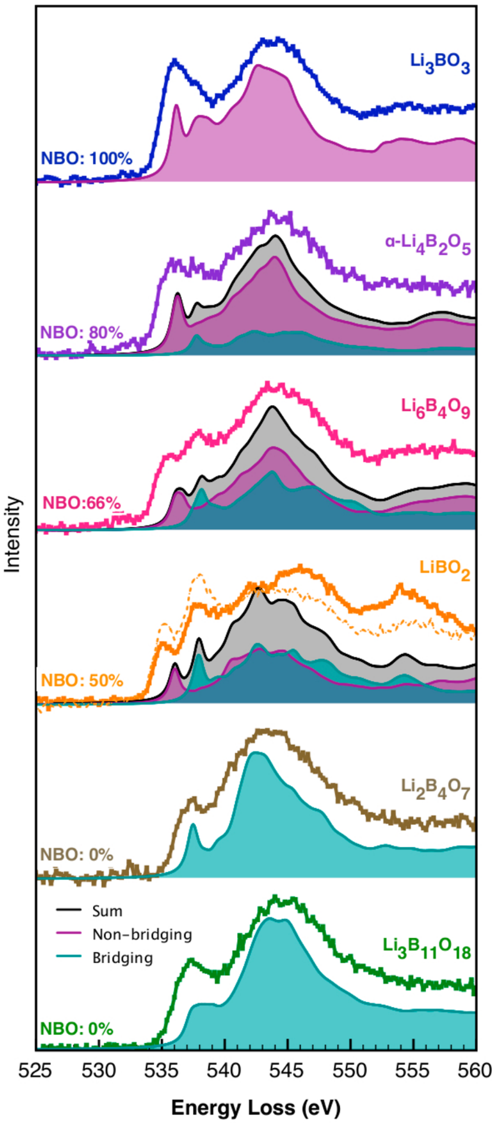

Figure 3. Experimental (colored symbols) and calculated (black lines) O K-edge NRIXS spectra for the six crystalline compounds. Blue and violet curves represent the respective contribution of the bridging oxygens and non-bridging oxygens (NBO) to the full spectrum. Gray-shaded area corresponds to the total calculated spectrum.

these atoms. The excitation energy calculated for a given site is closely related to the capability of the valence electrons to screen the locally more attractive potential of the ionized absorbing atom. Formation of iono−covalent bonds between neighboring atoms tends to delocalize the valence electron density (the 2s and 2p states in the case of oxygen) along these spatially oriented bonds and therefore to reduce the efficiency of this screening.

The O K-edge spectra appear to be a very sensitive probe of the presence of NBOs in borate sample. The specific signature of these atoms, i.e., a low-energy peak located at the edge onset is due to a large core-level shift separating the NBO and BO contributions by about 2 eV in the experiments.

Let us illustrate this point by the case of α-LiBO$_2$, a crystal containing only two crystallographically inequivalent oxygen sites corresponding to a bridging and non-bridging configuration. Figure 4 shows the screening density maps corresponding to the difference of the valence densities calculated for the ground-state and the XCH electronic configurations for the bridging oxygen atom in Figure 4a and for the non-bridging oxygen atom in Figure 4b. The main difference between these two maps consists in the larger deviation from spherical symmetry of the valence charge rearrangement in the case of the bridging atom induced by its covalent interaction with two neighboring boron atoms instead of one. The difference between the excitation energies calculated for these two atoms is 1.73 eV, in good agreement with the 2 eV separation found experimentally on the NRIXS O K-edge in α-LiBO$_2$.

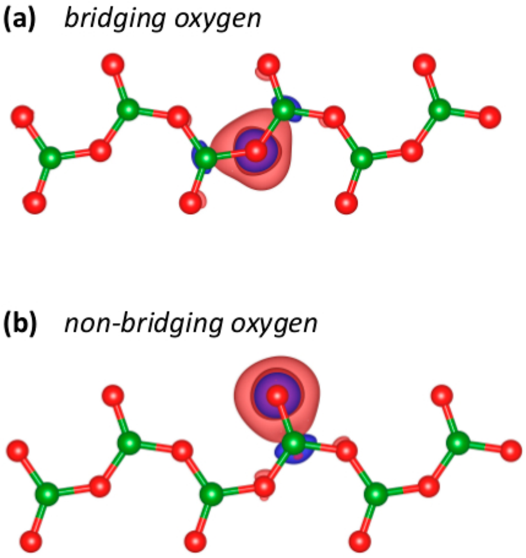

Figure 4. Calculated core−hole screening maps for a bridging oxygen (a) and non-bridging oxygen (b) in the case of LiBO$_2$. These maps correspond to the difference of valence electron densities calculated for the ground state and the XCH electronic configurations. The isosurface of 8.5 × 10^{-3} electron per Bohr^3 is shown. Red and blue surfaces indicate a deficiency or an excess of electron density, respectively.

In conclusion, both the O K-edge NRIXS measurements of the six crystalline lithium borate compounds and the theoretical calculations clearly demonstrated the presence of an additional feature at 535 eV originating from the non-bridging oxygen atoms. The intensity of this peak is directly related to the amount of NBO in lithium borates. This study highlights the great potentiality of NRIXS at the O K-edge as a unique tool to probe the oxygen sites without any isotopic enrichment. This opens research opportunities for structural characterization of a large variety of boron oxide materials that can be investigated by in situ O K-edge measurements in complex environments, such as high-pressure cells and high-temperature furnaces, together with a fully theoretical interpretation of the O K-edge spectra.

■ AUTHOR INFORMATION

Corresponding Author

*E-mail: gerald.lelong@impmc.upmc.fr.

Notes

The authors declare no competing financial interest.

■ ACKNOWLEDGMENTS

This work was granted access to the HPC resources of IDRIS under allocations 2013-100172 and 2014-100172 made by

GENCI (Grand Equipement National de Calcul Intensif). We acknowledge SOLEIL for provision of synchrotron radiation facilities (proposal 99130037).

■ REFERENCES

(1) Islam, M. M.; Bredow, T.; Heitjans, P. *J. Phys. Chem. C* **2011**, *115*, 7.

(2) Ohkubo, T.; Tsuchida, E.; Gobet, M.; Sarou-Kanian, V.; Bessada, C.; Iwadate, Y. *J. Phys. Chem. B* **2013**, *117*, 7.

(3) Lee, S. K. *Proc. Natl. Acad. Sci. U.S.A.* **2011**, *108*, 6.

(4) Stebbins, J. F. *Nature* **1997**, *390*, 3.

(5) Wright, A. C. *Phys. Chem. Glasses,. Eur. J. Glass Sci. Technol., Part B* **2010**, *51*, 39.

(6) Kroeker, S.; Aguiar, P. M.; Cerquiera, A.; Okoro, J. *Phys. Chem. Glasses: Eur. J. Glass Sci. Technol., Part B* **2006**, *47*, 393.

(7) Nesbitt, H. W.; Bancroft, G. M. *Rev. Mineral. Geochem.* **2014**, *78*, 271.

(8) Jiang, N. *Solid State Commun.* **2002**, *122*, 4.

(9) Jiang, N.; Silcox, J. *J. Non-Cryst. Solids* **2004**, *342*, 12.

(10) Jiang, N. *Solid State Commun.* **2002**, *122*, 4.

(11) Stebbins, J. F.; Zhao, P.; Kroeker, S. *Solid State Nucl. Magn. Reson.* **2000**, *16*, 9.

(12) Zhao, P.; Kroeker, S.; Stebbins, J. F. *J. Non-Cryst. Solids* **2000**, *276*, 10.

(13) Lee, S. K. *Solid State Nucl. Magn. Reson.* **2010**, *38*, 45.

(14) Lee, S. K.; Yi, Y. S.; Cody, G. D.; Mibe, K.; Fei, Y.; Mysen, B. O. *J. Phys. Chem. C* **2012**, *116*, 2183.

(15) Klie, R. F.; Walkosz, W.; Yang, G.; Zhao, Y. In *Scanning Transmission Electron Microscopy − Chapter 17: Variable Temperature Electron Energy-Loss Spectroscopy*; Pennycook, S. J., Nellist, P. D., Eds.; Springer: New York, 2011; pp 689−723.

(16) Massiot, D.; Fayon, F.; Montouillout, V.; Pellerin, N.; Hiet, J.; Roiland, C.; Florian, P.; Coutures, J.-P.; Cormier, L.; Neuville, D. R. *J. Non-Cryst. Solids* **2008**, *354*, 249.

(17) Pautler, B. G.; Colla, C. A.; Johnson, R. L.; Klavins, P.; Harley, S. J.; Ohlin, C. A.; Sverjensky, D. A.; Walton, J. H.; Casey, W. H. *Angew. Chem., Int. Ed.* **2014**, *126*, 10122.

(18) Rueff, J.-P.; Shukla, A. *Rev. Mod. Phys.* **2010**, *82*, 847.

(19) Lee, S. K.; Eng, P. J.; Mao, H.-K.; Meng, Y.; Newville, M.; Hu, M. Y.; Shu, J. *Nat. Mater.* **2005**, *4*, 4.

(20) Lee, S. K.; Eng, P. J.; Mao, H.-K.; Shu, J. *Phys. Rev. B* **2008**, *78*, 6.

(21) Lelong, G.; Cormier, L.; Ferlat, G.; Giordano, V.; Henderson, G. S.; Shukla, A.; Calas, G. *Phys. Rev. B* **2012**, *85*, 134202.

(22) Wu, M.; Liang, Y.; Jiang, J.-Z.; Tse, J. S. *Sci. Rep.* **2012**, *2*, 5.

(23) Lee, S. K.; Eng, P. J.; Mao, H.-K. *Rev. Mineral. Geochem.* **2014**, *78*, 139.

(24) Yi, Y. S.; Lee, S. K. *Am. Mineral.* **2012**, *97*, 897.

(25) Touboul, M.; Penin, N.; Nowogrocki, G. *Solid State Sci.* **2003**, *5*, 1327.

(26) Rousse, G.; Baptiste, B.; Lelong, G. *Inorg. Chem.* **2014**, *53*, 6034.

(27) Mathews, M. D.; Tyagi, A. K.; Moorthy, P. N. *Thermochim. Acta* **1998**, *320*, 7.

(28) Mathews, M. D.; Tyagi, A. K.; Moorthy, P. N. *Thermochim. Acta* **1998**, *319*, 9.

(29) Sennova, N.; Bubnova, R.; Shepelev, J.; Filatov, S.; Yakovleva, O. *J. Alloys Compd.* **2007**, *428*, 7.

(30) He, M.; Okudera, H.; Simon, A.; Köhler, J.; Jin, S.; Chen, X. *J. Solid State Chem.* **2013**, *197*, 5.

(31) Kirfel, A.; Will, G.; Stewart, R. F. *Acta Crystallogr.* **1983**, *B39*, 11.

(32) Lei, L.; He, D.; He, K.; Qin, J.; Wang, S. *J. Solid State Chem.* **2009**, *182*, 7.

(33) Stewner, V. F. *Acta Crystallogr.* **1971**, *B27*, 7.

(34) Rueff, J.-P.; Ablett, J.; Céolin, D.; Prieur, D.; Moreno, T.; Balédent, V.; Lassalle-Kaiser, B.; Rault, J.; Simon, M.; Shukla, A. *J. Synchr. Rad.*, To be published.

(35) Giannozzi, P.; Baroni, S.; Bonini, N.; Calandra, M.; Car, R.; Cavazzoni, C.; Ceresoli, D.; Chiarotti, G. L.; Cococcioni, M.; Dabo, I.; Dal Corso, A.; de Gironcoli, S.; Fabris, S.; Fratesi, G.; Gebauer, R.; Gerstmann, U.; Gougoussis, C.; Kokalj, A.; Lazzeri, M.; Martin-Samos, L.; Marzari, N.; Mauri, F.; Mazzarello, R.; Paolini, S.; Pasquarello, A.; Paulatto, L.; Sbraccia, C.; Scandolo, S.; Sclauzero, G.; Seitsonen, A. P.; Smogunov, A.; Umari, P.; Wentzcovitch, R. M. *J. Phys.: Condens. Matter* **2009**, *21*, 395502.

(36) Troullier, N.; Martins, J. L. *Phys. Rev. B* **1991**, *43*, 1993.

(37) Kleinman, L.; Bylander, D. *Phys. Rev. Lett.* **1982**, *48*, 1425.

(38) Perdew, J. P.; Burke, K.; Ernzerhof, M. *Phys. Rev. Lett.* **1996**, *77*, 3865.

(39) Taillefumier, M.; Cabaret, D.; Flank, A.-M.; Mauri, F. *Phys. Rev. B* **2002**, *66*, 195107.

(40) Gougoussis, C.; Calandra, M.; Seitsonen, A.; Brouder, C.; Shukla, A.; Mauri, F. *Phys. Rev. B* **2009**, *79*, 205105.

(41) Bunău, O.; Calandra, M. *Phys. Rev. B* **2013**, *87*.

(42) Blöchl, P. E. *Phys. Rev. B* **1994**, *50*, 17953.

(43) Pascal, T. A.; Boesenberg, U.; Kostecki, R.; Richardson, T. J.; Weng, T.-C.; Sokaras, D.; Nordlund, D.; McDermott, E.; Moewes, A.; Cabana, J.; Prendergast, D. *J. Chem. Phys.* **2014**, *140*, 034107.